Nanoscale

Accepted Manuscript

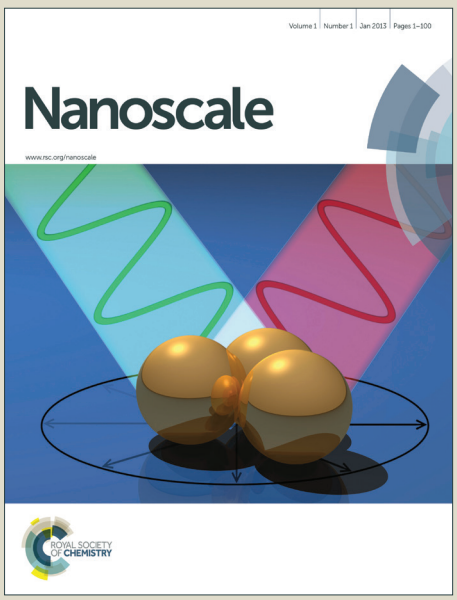

ROYAL SOCIETY OF CHEMISTRY

www.rsc.org/nanoscale

Article type: Full Paper

Table of contents:

Ferrite nanoparticles extracellularly synthesized by the bacteria *Geobacter sulfurreducen* show great potential for Nanomedicine. These nanoparticles may allow both diagnostics and controlled hyperthermia in the biological environment.

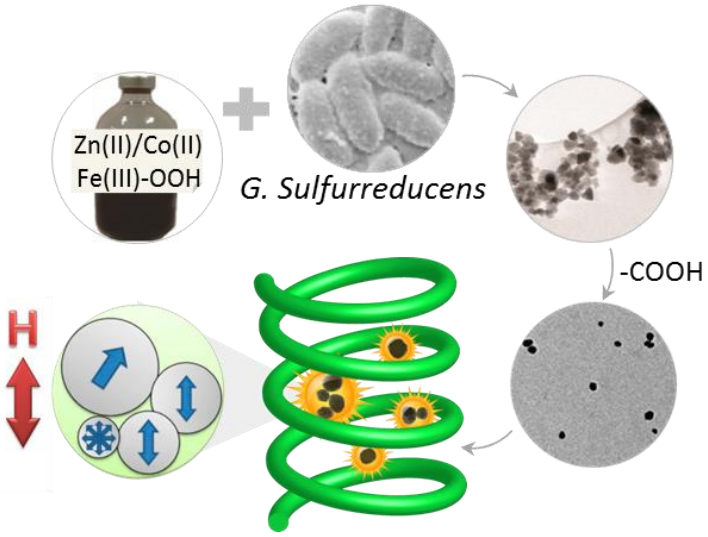

ToC Figure

Topic: Synthesis, characterization and manipulation of nanomaterials

Bacterially synthesized ferrite nanoparticles for magnetic hyperthermia applications

Eva Céspedes[1,†,*], James M. Byrne[2], Neil Farrow[1], Sandhya Moise[1], Victoria S. Coker[3], Martin Bencsik[4], Jonathan R. Lloyd[3] and Neil D. Telling[1]

[1]*Institute for Science and Technology in Medicine (ISTM), Keele University, Stoke-on-Trent ST4 7QB, UK*

[2] *Eberhard Karls Universitaet Tuebingen, Center for Applied Geoscience (ZAG), Tuebingen, Germany*

[3] *Williamson Research Centre for Molecular Environmental Science and School of Earth Atmospheric and Environmental Sciences (SEAES), University of Manchester, Manchester, UK*

[4] *College of Arts and Science, School of Science & Technology, Nottingham Trent University, Burton Street, Nottingham NG1 4BU,UK*

† Present address: Fundación Imdea Nanociencia, Faraday 9, Cantoblanco 28049 Madrid, Spain

[*] Corresponding-Author: e.cespedes@keele.ac.uk

Keywords: magnetic hyperthermia, magnetosomes, magnetic relaxation, AC susceptibility, *Geobacter sulfurreducens*.

ABSTRACT

Magnetic hyperthermia uses AC stimulation of magnetic nanoparticles to generate heat for cancer cell destruction. Whilst nanoparticles produced inside magnetotactic bacteria have shown amongst the highest reported heating to date, these particles are magnetically blocked so that strong heating only occurs for mobile particles, unless magnetic field parameters far outside clinical limits. Here, nanoparticles extracellularly produced by the bacteria *Geobacter sulfurreducens* are investigated that contain Co or Zn dopants to tune the magnetic anisotropy, saturation magnetization and nanoparticle sizes, enabling heating within clinical field constraints. The heating mechanisms specific to either Co or Zn doping are determined from frequency dependent specific absorption rate (SAR) measurements and innovative AC susceptometry simulations that use a realistic model concerning clusters of polydisperse nanoparticles in suspension. Whilst both particle types undergo magnetization relaxation and show heating effects in water under low AC frequency and field, only Zn doped particles maintain relaxation combined with hysteresis losses even when immobilized. This magnetic heating process could prove important in the biological environment where nanoparticle mobility may not be possible. Obtained SARs are discussed regarding clinical conditions which, together with their enhanced MRI contrast, indicate that biogenic Zn doped particles are promising for combined diagnostics and cancer therapy.

1. Introduction

In synergy with chemotherapy or radiotherapy, the localized heating effect produced by magnetic nanoparticles (MNPs) can be used for specific targeting and destruction of tumor cells.[1,2] By heating above 42°C, cancerous cells can be selectively damaged without harming the surrounding healthy tissue. Therapies based on this magnetic hyperthermia effect, now in clinical phase II trials, have already been proven in several types of cancer such as brain tumor,[1,3,4] prostate cancer[3,5] or breast carcinoma.[6,7]

The overall heating produced by the MNPs under an AC field is defined by the specific absorption rate (SAR). [8] Large SAR is essential to realize the therapeutic potential of this technique, where the applied field amplitude and frequency are limited by practical and clinical considerations.[2,9] Remarkably, magnetite nanocrystals synthesized in magnetosomes by magnetotactic bacteria, exhibit among the largest reported SAR values.[10,11,12,13] As well, their *in vivo* potential has recently been demonstrated in breast cancer in mice. By using ~ 1 mg of chains of bacterially synthesized magnetosome derived particles within the tumor and applying a considerably large magnetic field of 40 mT at 183 kHz three times during 20 min, complete regression of the tumor was observed.[6] Other types of MNPs such as cubed shaped nanoparticles,[14] hybrid core-shell MNPs like Fe_3O_4@$CaMoO_4$:Eu[15] and Fe_3O_4@YPO_4:Eu[16] or multigrain structures (nanoflowers)[17] have been recently investigated for magnetic hyperthermia showing also promising heating ability.

Heating efficiency depends strongly on particle and hydrodynamic (e.g. cluster) size distributions in nanoparticle suspensions, together with the magnetic characteristics of the particles.[8,18,19,20] Relaxation processes perturb the alignment of the magnetic moment by either the physical rotation of magnetically blocked MNPs (Brown relaxation) within the solution, or

the thermal randomization of magnetic moments within superparamagnetic (SPM) particles (Néel relaxation). If the period of an applied AC magnetic field becomes shorter than the Néel relaxation time, NPs are no longer SPM and magnetic hysteresis losses can occur.[21,22] While Néel and hysteresis processes are independent of the environment, Brown relaxation depends on the viscosity of the surrounded media, which might differ in biological conditions.[23] The experimental situation can be complex since MNPs and cluster distributions are typically broad. In this case, SPM particles may coexist with blocked single domain particles, and hysteresis losses may become significant at sufficient field amplitude.[22,24] In fact, an optimal magnetic hyperthermia effect should be possible beyond the SPM size range.[21] The ability to control magnetic anisotropy together with nanoparticle sizes could allow the optimization of the relaxation time for a specific frequency, thus greatly enhancing the heating effect (SAR).

Different methods can be used to synthesize magnetic nanoparticles, such as co-precipitation, hydrothermal approaches or ball milling. These are typically both economically and environmentally undesirable, due to the high temperatures and toxic chemicals involved. Instead, Fe(III) reducing bacteria are able to produce large amounts of extracellular magnetite at room temperature through the oxidation of an electron donor (organic matter or hydrogen), coupled with the reduction of metal cations such as Fe(III). [25,26] Furthermore, previous X-ray Magnetic Circular Dichroism (XMCD) investigations indicate that well-ordered doped magnetite nanoparticles can be biogenically produced,[27,28] which is crucial for the control of the magnetic anisotropy and thus optimization of the SAR.

Here we have explored the potential of three original types of bacterially produced MNPs (undoped magnetite, and Co- and Zn-doped ferrites) for magnetic hyperthermia. Of particular novelty, instead of magnetosome derived particles we have investigated extracellular MNPs

produced by the Fe(III)-reducing subsurface bacterium *Geobacter sulfurreducens*.[25,26] Smaller, SPM particles have successfully been obtained extracellularly which overcome the difficulties associated with the large magnetically blocked crystals which form within magnetosomes.[29,30] Such large particles, which are blocked even in static magnetic fields, are difficult to maintain in stable suspension and tend to aggregate, making them less suitable for biomedical applications. Another advantage is the ability to generate much larger quantities of the extracellularly produced particles compared to intracellular magnetosome nanoparticles produced at lower yields by magnetotactic bacteria. This enables a cost-effective scale-up of the process.

Although successful doping of intracellular biogenic nanoparticles has been reported only rarely,[31] through our recent work on extracellular biogenic nanoparticles we have shown that magnetic properties can be tuned by doping with transition metals[27,28] while controlling nanoparticle size through biomass manipulations. For Co-ferrites, coercivity was found to increase strongly with cobalt doping with a concurrent minor decrease of M_S and a large anisotropy enhancement (up to 4.8 x 10^5 J/m^3).[27] Conversely, by zinc doping we were able to enhance dramatically the saturation magnetization, M_S, reaching nearly 100 emu g^{-1} at RT whilst maintaining a low anisotropy (about 2 x 10^4 J/m^3).[28] These results are significant for the current study as both the magnetic properties and the particle sizes determine the dynamic (i.e. frequency dependent) magnetic behavior and consequently heating properties of the suspensions.

This work is focused on the SAR investigation of three unexplored magnetic nanoparticles extracellularly produced by bacteria (undoped magnetite and Co- and Zn-doped ferrites) and demonstrates their cancer therapy potential. The heating efficiency, measured under applied AC field conditions applicable to the clinical trials, is related to the derived roles of particle and cluster size distributions together with changes in magnetic anisotropy caused by metal doping.

AC magnetic susceptibility is used here as a powerful tool to gain further insight into the relaxation processes leading to magnetic self-heating at the hyperthermia frequencies. In combination with experimental data measured in different fluid viscosities, simulations of realistic model nanoparticle suspensions, which accurately reproduce experimental trends, are used to investigate the effect of size distributions (of both particles and particle clusters) and magnetic characteristics of the polydisperse suspensions. The obtained results are of broad interest for the extensive research community in the field of magnetic nanoparticles. For these biogenic nanoparticle suspensions, by suitable choice of metal dopant and concentration, we show that it is possible to tune the relaxation mechanisms from predominantly Brown relaxation, through mixed relaxation mechanisms, to predominantly Néel relaxation.

Large SAR values (over 250 W/ g_{Fe}) emerging from Brown relaxation are measured at 87 kHz and 20 mT. Of particular interest, Néel relaxation combined with hysteresis losses yields a persistent SAR above 40 W/g_{Fe} in immobilized Zn-doped MNPs at the same low frequency and field. This self-heating mechanism, which persists in glycerol, might be of fundamental importance to control magnetic heating processes *in vivo*. Additionally, the superior magnetic resonance imaging (MRI) contrast enhancement[28] shown for these biogenic nanoparticles compared to standard contrast agents, points out their clinical potential. These promising nanoparticles may be detected by MRI and reliably heated under an AC magnetic field independently of the milieu, allowing both diagnosis at any stage and controlled hyperthermia therapy.

2. Results and Discussion

2.1. Characterization of nanoparticle suspensions

TEM investigations (**Figure 1**) and dynamic light scattering (DLS) measurements were performed here to ensure accurate evaluation of both particle and cluster (particle aggregate) size distributions for the citric acid (CA) coated biogenic suspensions to be used for magnetic hyperthermia.

The size distribution of the particles was determined by measurement of 500 particles per sample from TEM images of concentrated solutions using ImageJ software (insets to **Figure 1**). Dilute samples were also investigated (**Figure 1**) in order to observe cluster characteristics in the absence of agglomeration artefacts caused by the drying concentrate (as seen in the insets to **Figure 1**). Dispersed nanoparticle clusters were observed to typically contain between one and four nanoparticles. The CA coating, distinguishable in **Figure 1f**, was evaluated by high resolution TEM (inset) and had an average thickness of 2.9 ± 1 nm.

Particle size distribution curves, together with DLS measurements of the hydrodynamic cluster sizes, are shown in **Figure 2**. As found in our previous investigations, the mean particle size and dispersion parameters depend on the metal dopant used (Zn or Co) with higher dopant concentrations yielding smaller particles.[27,28] For magnetic hyperthermia we examined the low doped samples, $Co_{0.4}$ and $Zn_{0.2}$ with corresponding mean particle diameters of 13.4 nm and 14.3 nm respectively; and the high doped samples, $Co_{0.7}$ and $Zn_{0.4}$ with respective diameters of 7.9 nm and 10.2 nm (**Figure 2b** and **2c**). Two different undoped biogenic magnetite suspensions were also measured (**Figure 2a**). The mean nanoparticle cluster (aggregate) size was found to range from 26 nm to 69 nm (**Figure 2d-f**) which compares well with the clusters observed in TEM images of the dilute suspensions (**Figure 1**). Both nanoparticle and cluster size distributions were described well by a log-normal distribution (**Figure 2**). The sample compositions and size

dispersion characteristics are summarized in **Table 1**, together with the measured saturation magnetization and estimated anisotropy constants.

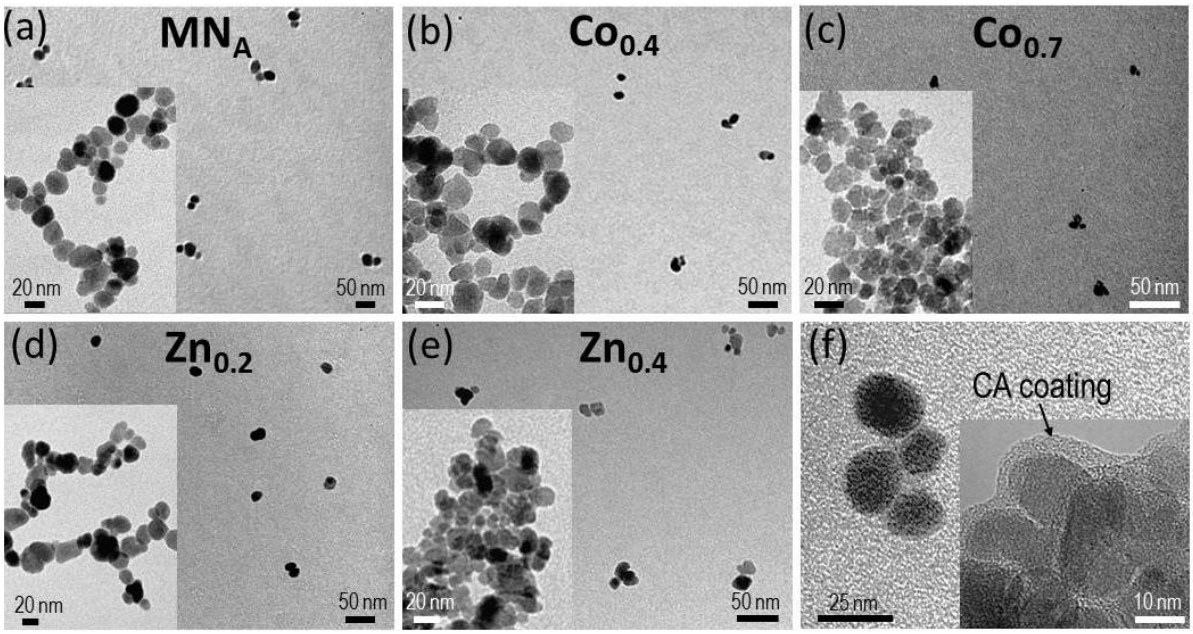

Figure 1. TEM images of citric acid (CA) coated biogenic nanoparticles: magnetite nanoparticles (MN_A) (a), Co-doped ferrite nanoparticles $Co_{0.4}$ (b) and $Co_{0.7}$ (c) and Zn-doped ferrite nanoparticles $Zn_{0.2}$ (d) and $Zn_{0.4}$ (e). Main micrographs (dispersed NPs aggregates) correspond to highly diluted samples. Insets show concentrated NPs samples. An example of NPs cluster (from $Zn_{0.2}$) where CA coating can be distinguished is shown in (f) and high resolution TEM (from concentrated $Co_{0.4}$) as the inset.

Table 1. (Top) Summary of structural and magnetic properties of most relevant biogenic samples. D is mean nanoparticle size; $\sigma_{(D)}$ is its dispersion index, D_H is mean hydrodynamic size, $\sigma_{(DH)}$ is its dispersion index, Ms RT is saturation magnetization at room temperature and K, magnetic anisotropy estimated considering uniaxial anisotropy. (Bottom) Structural and magnetic parameters from AC magnetic susceptibility simulations at 310 K of same samples. Values have been obtained from simultaneous simulation of experimental susceptibility spectra of each sample in water and glycerol, using same parameters in both except viscosity ($\eta_{water\ (310K)} = (7 \pm 0.5)\ x10^{-4}$ Pas, $\eta_{glyc\ (310K)} = 0.35 \pm 0.05$ Pas).

Sample label	Composition	D (nm)	$\sigma_{(D)}$	D_H (nm)	$\sigma_{(DH)}$	M_S RT (emu/cm^3)	K (J/m^3)
MN_A	Fe_3O_4	16.1 ± 0.1	0.25	52 ± 5	0.28	333	1.35 x 10^4
MN_B	Fe_3O_4	13.3 ± 0.1	0.23	69 ± 5	0.16	310	1.04 x 10^4
$Co_{0.4}$	$Co_{0.42}Fe_{2.58}O_4$	13.4 ± 0.1	0.27	31 ± 5	0.23	395	4.8 x 10^5
$Co_{0.7}$	$Co_{0.71}Fe_{2.58}O_4$	7.85 ± 0.1	0.27	26 ± 5	0.22	365	4.6 x 10^5
$Zn_{0.2}$	$Zn_{0.16}Fe_{2.84}O_4$	14.3 ± 0.2	0.26	29 ± 5	0.26	504	1.6 x 10^4
$Zn_{0.4}$	$Zn_{0.42}Fe_{2.58}O_4$	10.2 ± 0.1	0.25	38 ± 5	0.29	374	1.35 x 10^4
AC Susceptibility Simulation							
MN_A		16.1	0.25	49	0.29	333	1.1 x 10^4
MN_B		13.3	0.23	72	0.30	310	1.5 x 10^4
$Co_{0.4}$		13.4	0.27	23	0.36	395	4.6 x 10^5
$Co_{0.7}$		7.85	0.27	22	0.31	365	3.6 x 10^5
$Zn_{0.2}$		14.3	0.27	28	0.32	504	1.8 x 10^4
$Zn_{0.4}$		10.2	0.25	44	0.29	374	2.7 x 10^4

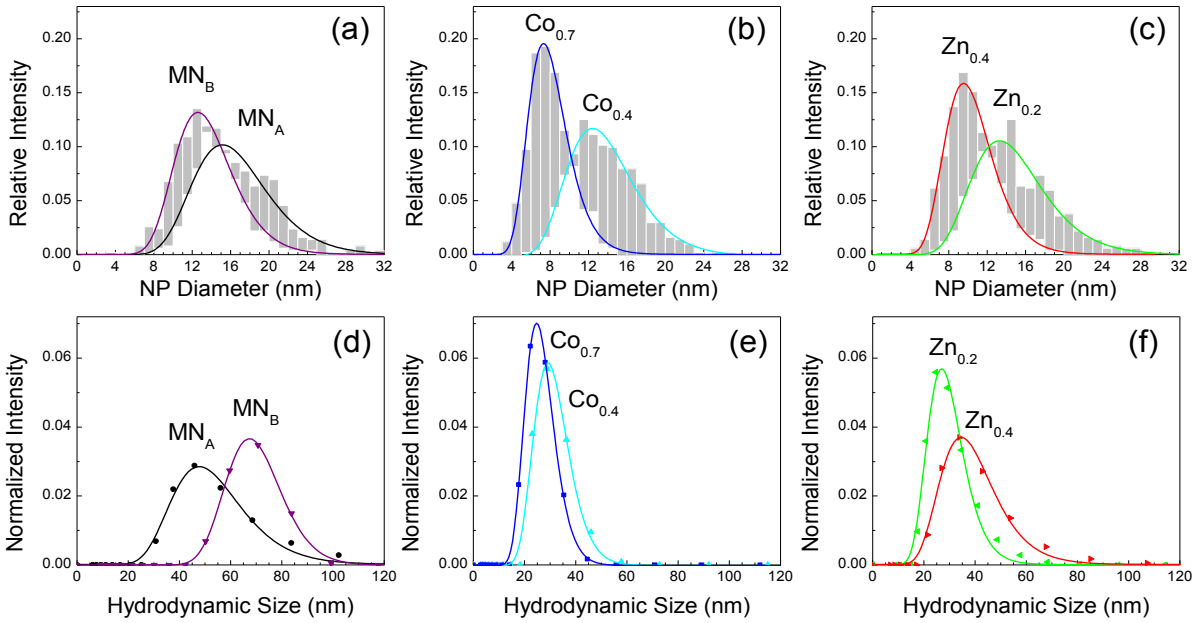

Figure 2. (color on-line) (Top) Size distributions obtained from TEM measurement of n=500 particle diameters per sample of (a) magnetite nanoparticles, (b) Zn-doped ferrite nanoparticles and (c) Co-doped ferrite nanoparticles. (Down) Normalized number-weighted hydrodynamic size distributions of CA-coated nanoparticles suspensions ((d), (e) and (f), from (a), (b) and (c), respectively) obtained by Dynamic Light Scattering measurements.

2.2. AC susceptibility of nanoparticle suspensions

In order to understand the dynamic magnetic behavior at frequencies of relevance to magnetic hyperthermia, we evaluated the AC magnetic susceptibility of the biogenic nanoparticle suspensions. The measured susceptibility of suspensions prepared with different solution viscosities was compared to simulated data. From this we derived the roles of particle/cluster size distributions together with changes in magnetic anisotropy caused by metal doping, on the dominant relaxation mechanism in the suspensions.

To simulate the AC susceptibility we used a model that takes into account a realistic polydisperse population of clusters containing nanoparticles of varying sizes taken from a

polydisperse population of particles (see **Figure S1**, Supporting Information). The susceptibility of each cluster was then calculated as the sum of the susceptibilities of each particle within the host cluster. Depending on the nanoparticle characteristics and the frequency of the applied magnetic field, either blocked or superparamagnetic behavior will be observed. Specifically, low frequencies of magnetic field will match the Brownian relaxation of the larger magnetically blocked particles, contributing to susceptibility, while smaller particles will appear superparamagnetic (not matched) at these frequencies. On the other hand, for intermediate frequencies, Néel relaxations of small superparamagnetic particles will be now matched while the magnetically blocked larger particles or the very small superparamagnetic (not matched) particles will not show any contribution to the total susceptibility. By introducing the desired inputs for nanoparticle population (mean particle size, D, and polydispersivity $\sigma_{(D)}$), cluster population (D_H and $\sigma_{(DH)}$), magnetic properties (anisotropy, K, and saturation magnetization, M_S), and temperature and viscosity, the AC susceptibility spectrum could be calculated for the model polydisperse suspension. For full details of the calculations see Supporting Information.

To illustrate the effect of both particle and cluster size distributions on the AC susceptibility of a typical polydisperse suspension, we used this model to calculate the susceptibility from a fixed population of nanoparticle clusters whilst allowing the anisotropy constant to vary (**Figure 3**). At the low and high anisotropy extremes the relaxation is dominated by Néel (**Figure 3a**) or Brown (**Figure 3f**) mechanisms respectively, with the peak in χ'' found at a position corresponding to the mean particle diameter (Néel) or mean cluster diameter (Brown). However, between these extremes (**Figures 3b-e**) some particles in the dispersion will be sufficiently large to induce Brown relaxation within their host clusters, provided that the anisotropy constant is high enough. Thus the susceptibility is a superposition of the behavior of individual particles within clusters,

and the overall frequency curve depends on the dispersion of both particle and cluster sizes. This can lead to some subtle effects that can be overlooked in measured AC susceptibility curves. For example an apparent Brown relaxation response can be obtained in which the χ' and χ'' curves do not cross at the frequency predicted by the linear relaxation theory (see for e.g**. Figure 3e**). See for instance Figure 9 of ref. [32].

Hence by suitable choice of metal dopant and by varying dopant concentration, it is possible to tune the relaxation mechanisms in these biogenic nanoparticle suspensions from predominantly Brown relaxation, through mixed relaxation mechanisms, to predominantly Néel modes of relaxation. The mean cluster sizes and dispersion indices, together with the anisotropy constants determined from the model fitting, are given in **Table 1** for undoped biogenic magnetite and for Co and Zn doped nanoparticle suspensions.

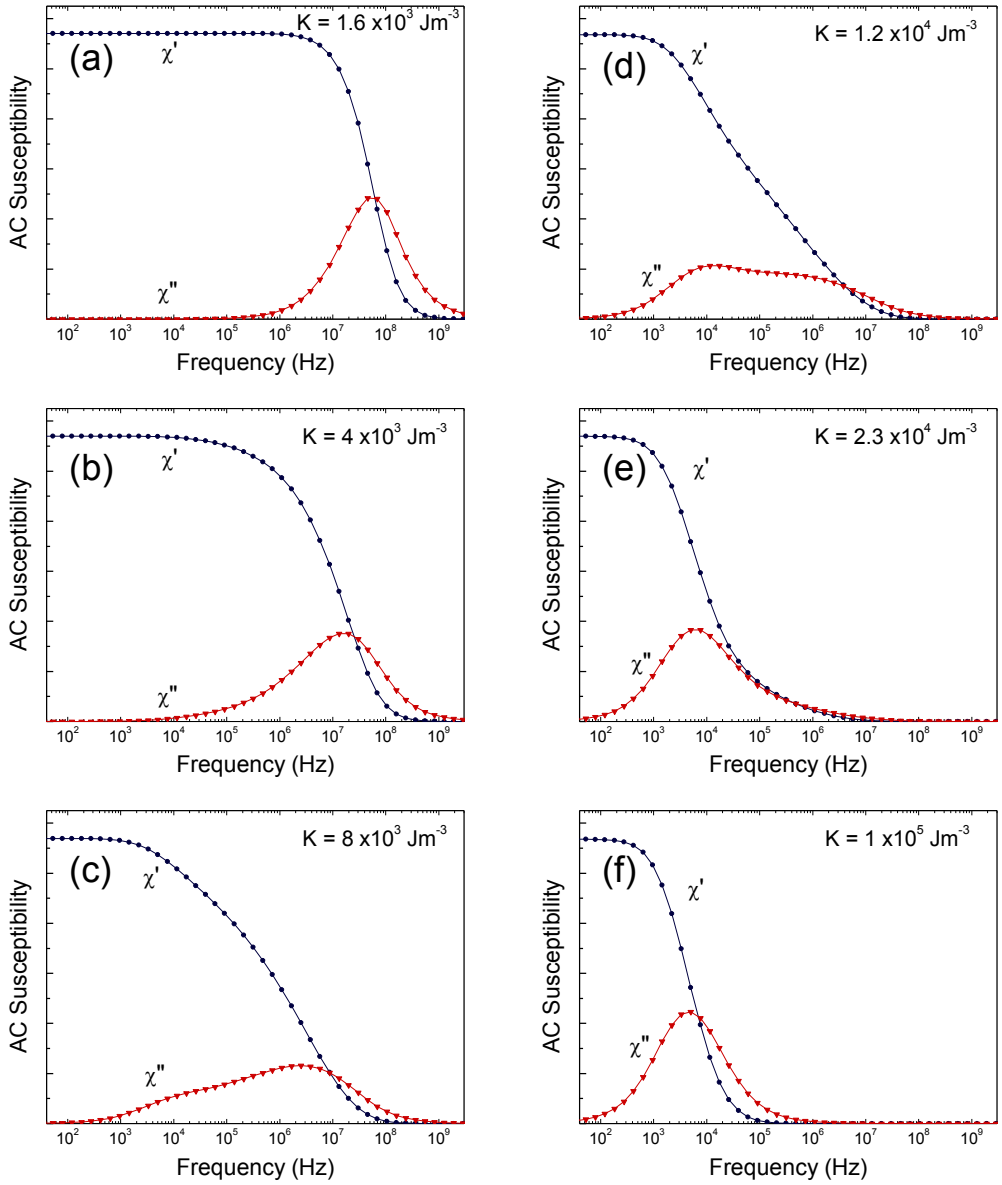

Figure 3. (color on-line) AC Susceptibility simulations showing the evolution from pure Néel (a) to pure Brown (f) relaxation for a selected NP distribution (D = 15.5 nm, $\sigma_{(D)}$ = 0.2) with cluster distribution (D_H = 40 nm, $\sigma_{(DH)}$ = 0.30) by increasing anisotropy constant (K). Simulations have been done for water at 310 K ($\eta = 7 \times 10^{-4}$ Pa s).

The measured AC susceptibility obtained from suspensions of Co or Zn doped biogenic nanoparticles as a function of solution viscosity, is shown in **Figure 4**. Corresponding simulated data obtained from the model discussed above are also shown in this figure. For the simulated

data, the particle sizes and saturation magnetization are assumed from measured values, but other parameters were varied to obtain the best qualitative fit of the spectra for all viscosities used.

According to the usual equation for Brown relaxation, $t^B = \frac{4\pi\eta D^3}{k_B T}$, the Brown relaxation time will increase with increasing viscosity, resulting in a shift in the χ'' peak to lower frequency values. This can clearly be seen in both the measured and simulated data for the Co doped sample (**Figure 4a** and **b**). The overlap of χ' and χ'' curves is also consistent with a single Brown relaxation mechanism, indicating that the suspension comprises clusters of nanoparticles that are all blocked within the measured frequency range, due to the high anisotropy constant of the cobalt ferrite (given in **Table 1**).

In contrast, a very different behavior is observed in the Zn doped nanoparticles (**Figure 4c**). In this case the χ' and χ'' curves do not cross within the measured frequency range. In addition, although the peak position in the χ'' curve shifts to lower frequency as before, its amplitude also diminishes as the viscosity is increased. This effect can be explained by considering the distribution of particle sizes within the clusters, together with their anisotropy. As the anisotropy constant is much lower in the Zn doped particles than the Co doped particles (**Table 1**), not all particles will be blocked within the measured frequency range. In particular, only the very largest particles within the distribution will be blocked in the lowest frequency regime to which the χ'' peak is shifted when the Brown relaxation time is enhanced (by increasing the viscosity). Thus the Brown relaxation component of the overall susceptibility will be maintained by a reduced proportion of the particle population at these lower measurement frequencies. This leads to the gradual suppression of the χ'' peak as the viscosity increases and indicates that the majority of the particles are blocked at a frequency near to that of the χ'' peak in water. This effect is also

reflected in the complex decay of the real component of the susceptibility across the measured frequency range (**Figure 4c**). The trend in the susceptibility curves from the Zn doped sample is remarkably well reproduced in the simulated data from the model (**Figure 4d**). Given that this model explicitly accounts for nanoparticle clusters formed from a population of different particle sizes, the reproduction of the trend with viscosity validates the explanation for the diminished Brown relaxation given above.

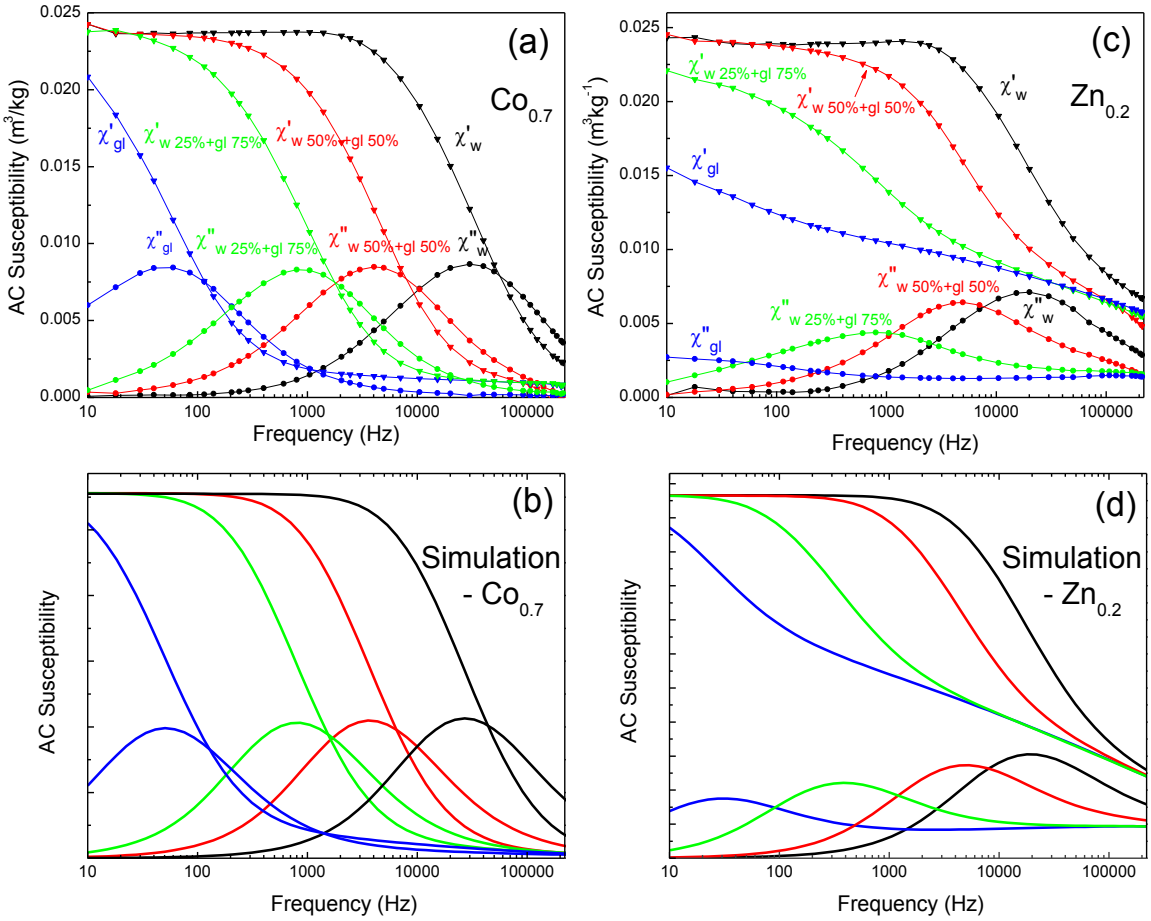

Figure 4. (color on-line) (Top) Experimental AC susceptibility spectra of $Co_{0.7}$ (a) and $Zn_{0.2}$ (c) coated nanoparticles suspended in water and different mixtures of water-glycerol (in volume; 50%-glycerol, 75%-glycerol and 100% glycerol). (Bottom) AC susceptibility simulations of $Co_{0.7}$ (b) and $Zn_{0.2}$ (d) by using the parameters summarized in **Table 1**. Viscosity input values are $\eta_{water\ (310K)} = (7 \pm 0.5)\ x10^{-4}$ Pas, $\eta_{50\%\text{-}glyc\ (310K)} = (4.5 \pm 0.5)\ x10^{-3}$ Pas, $\eta_{75\%\text{-}glyc\ (310K)} = (2 \pm 0.5)\ x10^{-2}$ Pas and $\eta_{glyc\ (310K)} = 0.35 \pm 0.05$ Pas.

Further to these observations it can also be seen that both experimental and simulated curves in the Zn doped sample appear to converge at a frequency above the measured range (**Figure 4c** and **d**). This evidences the underlying Néel relaxation mechanism that has fixed frequency dependence irrespective of the solution viscosity.

A similar effect can be seen in the high doped Zn sample, $Zn_{0.4}$ (**Figure 5**) where again a close agreement between measured and simulated spectra can be observed. However for this sample only a weak χ'' peak is observed in water, indicating that a relatively small proportion of the particles are blocked at this frequency and that Néel relaxation is therefore the dominant relaxation mechanism for this sample. Additional evidence for this is found in the preservation of the real component of the susceptibility for the glycerol suspension up to the highest frequencies measured. Extending the simulated data beyond the measured frequency range (**Figure 5b**) reveals a broad χ'' peak that corresponds to the distribution of Néel relaxation times for the polydisperse particle size distribution. This peak is by definition broader than the peak corresponding to Brown relaxation of clusters, due to the exponential term in equation.

Hence by suitable choice of metal dopant and by varying dopant concentration, it is possible to tune the relaxation mechanisms in these biogenic nanoparticle suspensions from predominantly Brown relaxation, through mixed relaxation mechanisms, to predominantly Néel modes of relaxation. The mean cluster sizes and dispersion indices, together with the anisotropy constants determined from the model fitting, are given in **Table 1** for undoped biogenic magnetite, and for Co and Zn doped nanoparticle suspensions. Measured anisotropy values (top of the table) were estimated from previous magnetometry data using the expression $H_C = 0.958\ K/M_S$ (from ref [33] assuming uniaxial anisotropy), where H_C and M_S correspond to the coercivity and saturation magnetization at 5 K (from refs [26,27,28]), respectively. Generally a very good agreement can

be seen between measured values (cluster sizes and estimated anisotropy constants) and values obtained from the AC susceptibility simulations.

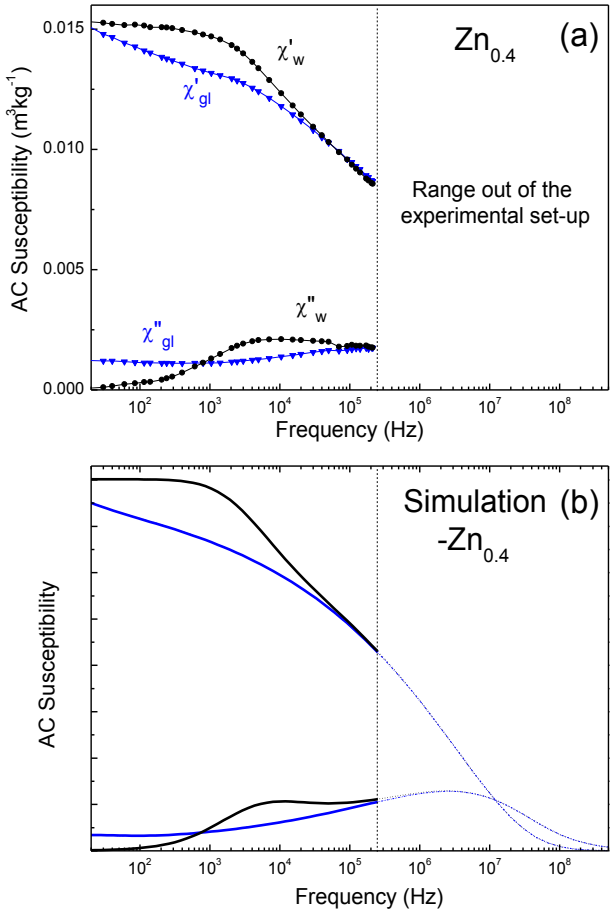

Figure 5. (color on-line) (a) Experimental AC susceptibility spectra of $Zn_{0.4}$ coated nanoparticles suspended in water and glycerol and their simulation (b) by using the parameters summarized in **Table 1** (bottom).

Results of the simulated susceptibility data beyond the measured frequency range for samples MN_A, $Zn_{0.2}$ and $Zn_{0.4}$ have been included in the Supporting Information (**Figures S6** and **S7**) to give further details of the Brown and Néel relaxations in these samples. The simulations also confirm the complete immobilization of the NPs in glycerol for the frequency range of magnetic hyperthermia used in these experiments.

2.3. Magnetic hyperthermia

Magnetic hyperthermia measurements were performed to determine the specific absorption rate (SAR) of the nanoparticle suspensions. The SAR was calculated from the rate of change of temperature of a suspension containing a known concentration of nanoparticles under the influence of an AC magnetic field using the formula $SAR = \frac{C\,V_S}{m}\frac{dT}{dt}$ where C is the volume specific heat capacity of the sample (C_{water} = 4185 J L^{-1} K^{-1}, $C_{glycerol}$ = 3086 J L^{-1} K^{-1}), V_s = 1 mL is the sample volume, and m is the mass of magnetic material. SAR values for undoped magnetite (MN), together with Co and Zn doped ferrites, suspended in water and glycerol, were determined for frequencies between 87 kHz and 998 kHz (**Tables 2** and **3**). Examples of the experimental heating curves can be found in the supporting information (**Figure S4**).

For the experimentally available frequencies and magnetic field amplitudes, the highest SAR values among the Co-series were obtained for $Co_{0.4}$ and $Co_{0.7}$ in water (253 W/g_{Fe} and 136 W/g_{Fe}, respectively, at 87 kHz and 20 mT). These values are considerably larger than those measured for the undoped magnetite nanoparticles which range from 25 to 60 W/g_{Fe} (MN_B and MN_A). However, from the AC susceptibility measurements discussed above, it was found that the high anisotropy constant of the Co ferrite nanoparticles was sufficient to block even the smallest particles in the distribution such that only Brown relaxation occurred. In fact for frequencies >20 kHz the χ'' component for Co ferrite nanoparticles immobilized in glycerol decays to zero (**Figures 4a** and **b**), leaving hysteresis losses as the sole contribution to the heating effect. As the anisotropy of these particles is high, only minor AC hysteresis loops will be obtained for the modest magnetic fields applied in the hyperthermia measurements, resulting in the drastic reduction in the SAR measured in glycerol (**Table 2**). For comparison, additional Co doped samples (labelled $Co_{0.38}$ and Co_1 in **Table 2**) that have larger hydrodynamic (cluster)

sizes (>100 nm) show only weak heating effects in water or glycerol, as neither Brown nor Néel relaxation mechanisms are optimum for the hyperthermia frequency range.

The energy loss per mass of iron during magnetic hyperthermia (from SAR values) normalized to H^2 and frequency in order to compare all the measured samples in water and glycerol is shown as supporting information (Figure S5).

Table 2. Summary of SAR for MN_B and $Co_xFe_{3-x}O_4$ samples suspended in water and in glycerol, at different frequencies ranging between 87 kHz and ~ 1MHz and at maximum magnetic field amplitude available. $\Delta f = \pm 5$ kHz; $\Delta B = \pm 0.5$ mT.

	SAR (W/g_{Fe})						
solvent	Water						
sample	f = 87 kHz B = 20 mT	f = 112 kHz B = 17 mT	f = 176kHz B = 11 mT	f = 238 kHz B = 8 mT	f = 375 kHz B = 8 mT	f = 746 kHz B = 4 mT	f = 998 kHz B = 3 mT
MN_B	25 ± 1	35 ± 1	30 ± 1	28 ± 1	44 ± 1	19 ± 1	13 ± 1
$Co_{0.38}$	48 ± 5	44 ± 3	21 ± 3	15 ± 3	25 ± 3	15 ± 3	8 ± 3
$Co_{0.4}$	253 ± 11	225 ± 10	110 ± 8	84 ± 8	104 ± 8	53 ± 7	39 ± 3
$Co_{0.7}$	136 ± 2	114 ± 2	65 ± 2	44 ± 2	54 ± 2	16 ± 2	11 ± 2
Co_1	10 ± 1	12 ± 1	7 ± 1	8 ± 1	15 ± 1	19 ± 1	7 ± 1
	glycerol						
MN_B	13 ± 1	12 ± 1	12 ± 1	15 ± 1	21 ± 1	16 ± 1	9 ± 1
$Co_{0.38}$	5 ± 2	2 ± 1	6 ± 2	8 ± 2	12 ± 2	8 ± 2	8 ± 2
$Co_{0.4}$	15 ± 4	8 ± 3	2 ± 3	8 ± 3	13 ± 3	8 ± 3	10 ± 3
$Co_{0.7}$	3 ± 1	3 ± 1	2 ± 1	3 ± 1	5 ± 1	3 ± 1	4 ± 1
Co_1	5 ± 1	5 ± 1	4 ± 1	4 ± 1	10 ± 1	4 ± 1	3 ± 1

Table 3. Summary of SAR for MN_A and $Zn_xFe_{3-x}O_4$ samples suspended in water and in glycerol, at different frequencies ranging between 87 kHz and ~ 1MHz and at maximum magnetic field amplitude available. $\Delta f = \pm 5$ kHz; $\Delta B = \pm 0.5$ mT. Note that the maximum magnetic field for frequencies between 263 kHz and 740 kHz is larger than in Table 2, being the same for 87 kHz, 112 kHz and 998 kHz.

	SAR (W/g_{Fe})					
solvent	water					
sample	f = 87 kHz B = 20 mT	f = 112 kHz B = 17 mT	f = 263 kHz B = 10.8 mT	f = 523 kHz B = 11.2 mT	f = 740 kHz B = 8 mT	f = 998 kHz B = 3 mT
MN_A	60 ± 2	60 ± 2	63 ± 2	74 ± 2	48 ± 2	22 ± 2
$Zn_{0.2}$	255 ± 10	223 ± 5	160 ± 8	240 ± 11	95 ± 7	45 ± 5
$Zn_{0.4}$	42 ± 2	54 ± 2	69 ± 2	117 ± 5	72 ± 2	40 ± 2
	glycerol					
MN_A	18 ± 1	19 ± 1	15 ± 1	31.5 ± 1	21 ± 2	5 ± 1
$Zn_{0.2}$	42 ± 3	24 ± 3	13.5 ± 3	29 ± 3	18 ± 3	10 ± 3
$Zn_{0.4}$	15 ± 1	18 ± 1	20 ± 1	34 ± 1	28 ± 1	8 ± 1

For the Zn doped series, a varying proportion of the particles is blocked within the frequency range depending on the combination of particle size and anisotropy constants. For the $Zn_{0.2}$ sample a significant proportion of the particles is blocked near to the lowest hyperthermia frequency measured at 87 kHz (see **Figure S7** in Supporting Information for details). As for the $Co_{0.4}$ sample, this leads to a substantial SAR in water of 255 W/g_{Fe} due mainly to Brown relaxation of the nanoparticle clusters. However as the Néel relaxation time for a significant proportion of the particles lies within this hyperthermia range, AC magnetic hysteresis losses should occur for the immobilized NPs even for the modest magnetic field that can be applied in the hyperthermia instrument. Hence a significant SAR of 42 W/g_{Fe} is retained when the suspension is immobilized in glycerol (**Table 3**).

Accordingly, SQUID magnetometry performed at 5K (to ensure a blocked state) on MN_A and the Zn-doped samples, evidenced small coercive fields in the range of 20 to 30 mT,[28] which are comparable to the magnetic field strength available for hyperthermia at the lowest frequencies (20 mT at 87 kH). Thus substantial hysteresis losses would be expected in this case. Conversely, Co-doped samples showed considerably large coercive fields at 5 K, above 500 mT, in agreement with their high anisotropy much larger than the typical magnetic fields used for hyperthermia treatments.

The presence of hysteresis loss heating can be demonstrated by examining the energy loss per cycle for the undoped magnetite and Zn doped samples, measured in glycerol (**Figure 6a**). At the lowest frequencies, an enhanced heating due to hysteresis losses can be seen for the $Zn_{0.2}$ sample that quickly diminishes at frequencies >100 kHz (**Figure 6a**). However, very similar heating trends are observed for all samples in this series at frequencies above 100 kHz. From the extended susceptibility simulations for these NPs immobilized in glycerol (**Figure 6b**), the broad high frequency peaks corresponding to Néel relaxation, occur above 100 kHz. Thus a proportion of particles remain in a superparamagnetic state between 100-1000 kHz and Néel relaxation based heating should play the dominant role as the field that can be applied at these frequencies is too small to generate hysteresis losses. In fact, above 100 kHz the heat loss for all samples follows a squared dependence with the applied field strength (**Figure 6a**), indicative of a relaxation based heating mechanism.

In contrast, for the Co doped series in glycerol almost no heating is observed above 100 kHz (**Table 2**), consistent with the lack of possible Néel relaxation or hysteresis losses for these samples. It should be noted that a complete inhibition of the Brownian relaxation in cellular conditions have been recently reported by Di Corato et al. [34] for different nanoparticles

designs. On the other hand the undoped magnetite suspension (MN_B) shows a similar response to the $Zn_{0.4}$ and MN_A particles in **Figure 6a**, suggesting a similar Néel relaxation mediated heating occurs in this sample.

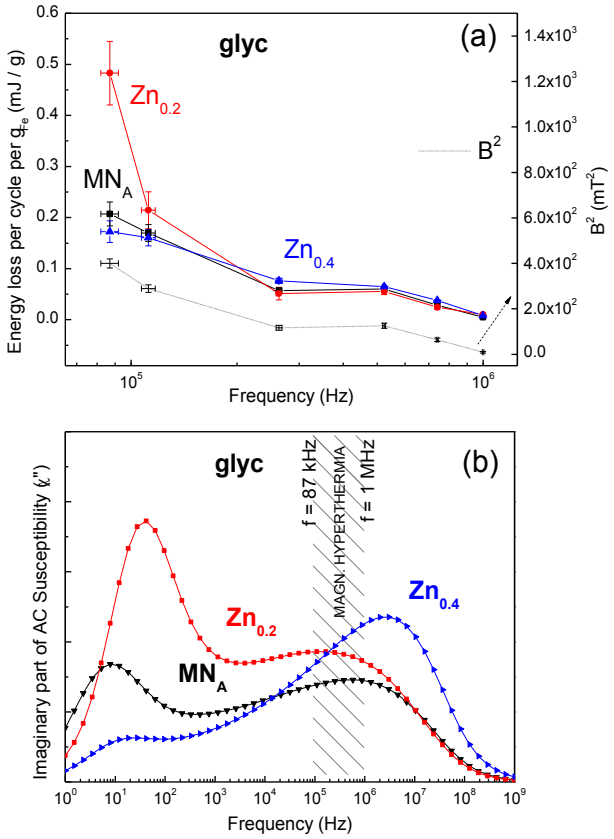

Figure 6. (a) Energy loss per cycle (mJ/g_{Fe}) during magnetic hyperthermia derived from SAR values measured in glycerol for MN_A and the Zn doped samples (b) Simulated χ" susceptibility of same samples in glycerol (using simulation parameters summarized in **Table 1**). Striped region shows the frequency range used for magnetic hyperthermia, from 87 kHz to 998 kHz.

Further evidence for Brown relaxation and hysteresis losses as the heating mechanisms for different particle types, was obtained by measuring the SAR as a function of applied magnetic field (**Figure 7**). Particles generating heat by a magnetization relaxation mechanism (of either

Brown or Néel origin) will show a squared dependence of the SAR with applied magnetic field.[21] From **Figure 7** it can be seen that all the particle types investigated obey nearly-square law behavior of SAR versus magnetic field when suspended in water (**Figure 7a-c**). However the $Zn_{0.2}$ particles immobilized in glycerol and measured at the lowest hyperthermia frequency (87 kHz) show a third order power law dependence of SAR with field (**Figure 7d**), suggesting that heating occurs in at least a proportion of the particles in the sample due to a non-relaxation based mechanism such as hysteresis losses. A greater than second order behavior was also found for the undoped magnetite sample (MN_A) at this frequency, indicating a component of the hysteresis loss heating also occurs in this sample, but from a smaller particle population.

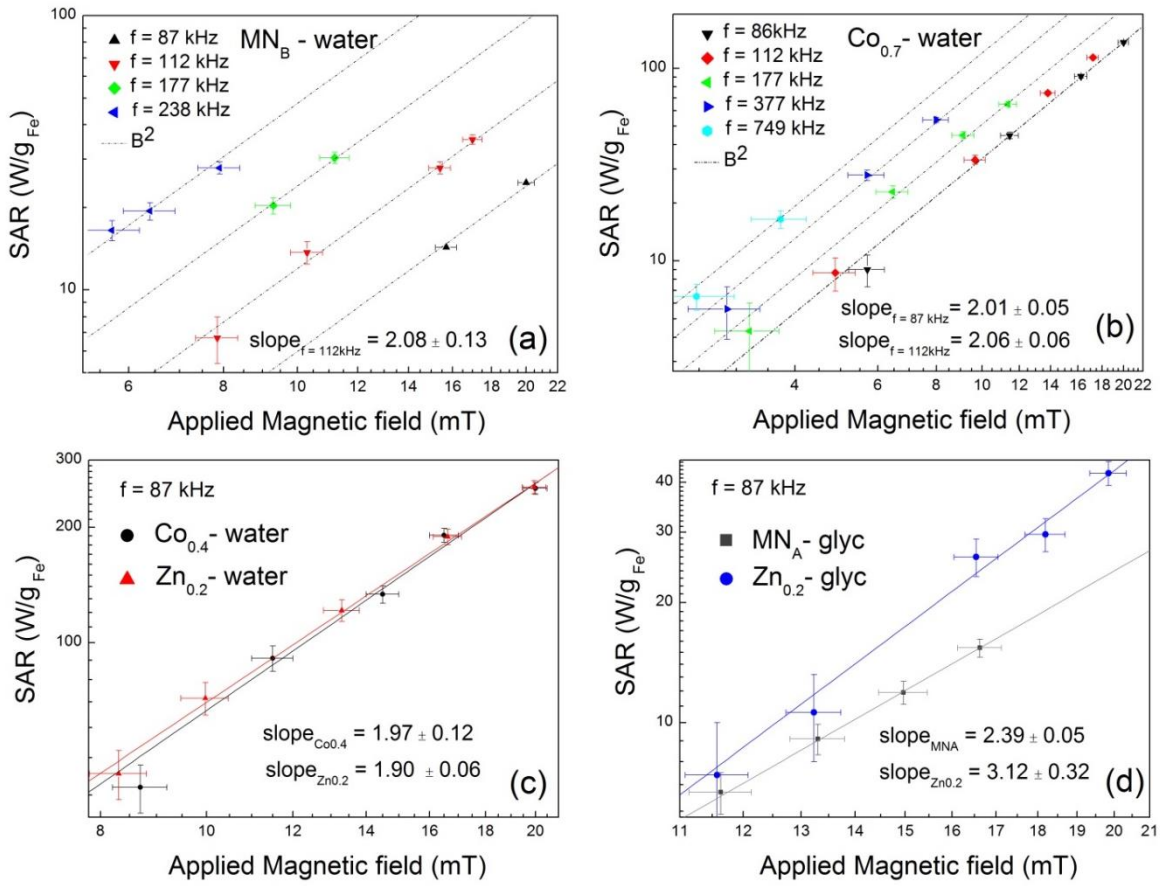

Figure 7. SAR dependence versus applied magnetic field for (a) MN_B and (b) $Co_{0.7}$ in water at different frequencies. In the log-log plots, the dashed line corresponds to a square dependence of SAR on the field amplitude (slope = 2). SAR versus applied magnetic field for the two samples showing the highest experimental SAR values ($Co_{0.4}$ and $Zn_{0.2}$ in water at 87 kHz). (d) SAR versus magnetic field dependence for MN_A and $Zn_{0.2}$ samples suspended in glycerol.

2.4. Clinical considerations: Hyperthermia of biogenic nanoparticles

It should be noted that in cells, a decrease in SAR might be expected either by the presence of magnetic particle-particle interactions (impacting on Néel relaxation) due to the confinement of the particles (affecting Brownian relaxation).[34]

Furthermore, for clinical use, the product of the frequency (f) and the applied magnetic field (H_0) should be limited to avoid non-localized temperature increase due to Eddy currents.[35] Although the safe condition was initially estimated as $H_0 f < 4.85 \times 10^8$ $Am^{-1}s^{-1}$ by Brezovich[9], a more relaxed limit of $H_0 f < 5 \times 10^9$ $Am^{-1}\,s^{-1}$ is now widely reported in the literature.[17,21,36, 37]

For a rough estimation, taking into account this more recent limit, 87 kHz would restrict the maximum field amplitude to ~45 mT. This allows an approximate SAR estimation by considering its square dependence with the field, in water (as shown in **Figure 7**). For $Zn_{0.2}$, this estimation leads to SAR of approximately 1330 W/g_{Fe} at 45.7 mT and 87 kHz in water. For glycerol, considering an assumed relationship SAR ~ H_0^3 (as found, shown in **Figure 7d**) the approximation would lead to ~500 W/g_{Fe}, in this case independently of the biological environment. Despite their particular relevance for biomedical applications, SAR values of immobilized MNPs have been hardly reported in the literature. Alphandéry et al.[13] have found SAR over 800 W/g_{Fe} for intact chains of bacterial magnetosomes immobilized in a gel due to hysteresis losses at 108 kHz, but for very large fields, 88 mT.

Owing to the different experimental conditions it is difficult to make direct SAR comparisons with published literature. For instance, Hergt found among the largest reported values, nearly 1 kW/g for magnetosomes at 410 kHz and 10 kA/m.[11] Considering the same $H_0 f$ product, our above rough estimation (for 87 kHz in water) would lead to a SAR value over 2 kW/g_{Fe}. On the other hand, SAR values of up to ~ 500 W/g_{Fe} were reported for cobalt doped chains of magnetosomes, when exposed to a field of 183 kHz and 80 mT[12] and above 1.2 kW/g_{Fe}, due to hysteresis plus rotation of chains of magnetosomes at 108 kHz and 88 mT.[13] These magnetic field amplitudes are in fact considerably larger than those considered safe for magnetic hyperthermia applications.

A more realistic limit might be inferred from the clinical trials carried out by Thiesen et al.[2] by direct injection of aminosilane-coated iron oxide nanoparticles in a number of patients with different types of tumors. Thermotherapy was carried out using an AC magnetic field applicator system operating at 100 kHz and variable field strength of 0–22.6 mT. Regarding this instrumental limit ($H_{0max} f < 1.8 \times 10^9$ $Am^{-1} s^{-1}$), our experimental limit is comparable, becoming smaller for f < 263 kHz. Thermotherapy was well tolerated in 14 patients suffering from glioblastoma multiforme up to ~ 17 mT at 100 kHz, analogous to our low frequency conditions. For recurrent and residual tumors (e.g. prostate and cervix carcinoma, soft tissue sarcoma) depending on the tumor location, tolerated fields were limited by local discomfort to smaller values (to 4–6 mT in the pelvic region and up to 10.7 mT in the upper thorax).

Another issue for clinical trials is the ability to track the nanoparticles *in vivo* using MRI. By combining diagnosis and magnetic hyperthermia therapy, the location of the magnetic self-heating dose can be monitored before each treatment, allowing observation of the tumor during and after therapy. For MRI, the contrast enhancement afforded by magnetic nanoparticles is an

important factor that determines the lower level of particle concentration that can be detected. We have previously shown that the transverse relaxation ($R_2 = 1/T_2$) for the biogenic Zn doped nanoparticles is around five times stronger than that of standard iron oxide based contrast agents [28]. In Fig. 8 we show, in addition to our previously published results, the T_2 weighted MRI images at a polarising field of 2.35 T for the Zn doped series suspended in agar gels, for low and high concentrations, in comparison with a standard MRI agent (Feridex®). Obtained R_2/R_1 values for these samples were ~9 for Feridex®, 13 for MN_A, 70 for $Zn_{0.2}$ and 19 for $Zn_{0.4}$. The increase in R_2 contrast (shortening of T_2, which ranges from 0 to 100 on the right scale) for the same concentration that can be seen in Fig. 8, demonstrates the enhanced contrast expected for *in vivo* imaging of these biogenic nanoparticles.

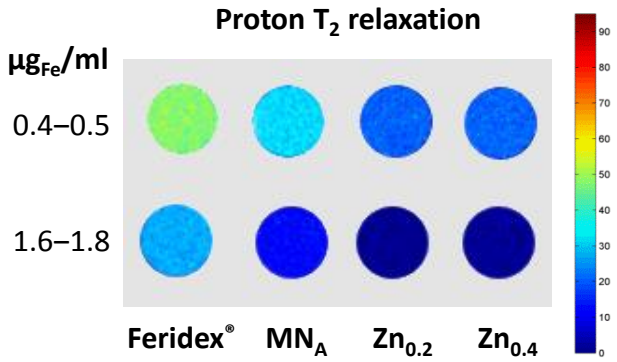

Figure 8. T_2-weighted MR images for undoped magnetite (MN_A) and Zn-doped ferrites $Zn_{0.2}$ and $Zn_{0.4}$ in comparison with a standard MRI contrast agent (Feridex®), for two different nanoparticles doses.

3. Conclusions

We have demonstrated the potential for magnetic hyperthermia applications using biogenic magnetic nanoparticles innovatively prepared by cultures of the bacterium *Geobacter sulfurreducens*. The successful doping of these particles with Co or Zn enabled the variation of the magnetic anisotropy, saturation magnetization and nanoparticle sizes, which leads to variations in the heating properties at different frequencies and in different environments.

Investigations of their dynamic magnetic behavior by AC susceptibility revealed differences in the relaxation mechanisms emerging from Co or Zn doping according to their magnetic and size characteristics. By suitable choice of metal dopant and concentration, tuning of the relaxation mechanisms from predominantly Brown, through mixed relaxation processes, to predominantly Néel, was shown.

Both particle types undergo Brown relaxation in water under low AC frequency and magnetic field (87 kHz, 20 mT) yielding relatively high SAR values of more than 250 W/g_{Fe} under realistic clinical conditions. For Zn doped particles, an additional significant Néel contribution has also been found. Just by doping with 5% of zinc, $Zn_{0.2}$, results in a very promising combination of the largest magnetic response (M_S = 504 emu/cm^3 at RT), an average hydrodynamic size below 30 nm and low K ~ 2 x 10^4 J/m^3. Despite its polydisperse nature, Néel relaxation combined with hysteresis losses led to a persistent SAR above 40 W/g_{Fe} when immobilized under the same conditions (87 kHz, 20 mT).

The self-heating mechanisms of these nanoparticles with minor Zn doping, which persist also in glycerol, could prove important for in vivo magnetic heating therapies where nanoparticle mobility cannot be guaranteed.

This, jointly with their shown superior MRI contrast enhancement, indicates the enormous potential of bacterially synthesized nanoparticles, which are prepared under an environmentally benign and scalable process, for both diagnostics and controlled hyperthermia therapy.

4. Experimental

4.1 Synthesis of biogenic nanoparticles (undoped and Zn and Co-doped ferrite NPs)

The synthesis procedures of biogenic Zn and Co doped magnetite nanoparticles are described in detail in references [27] and [28]. Briefly, *M*-Fe(III)-oxyhydroxide suspensions containing varying molar concentrations of Zn and Co were prepared through the co-precipitation of $FeCl_3$ and MCl_2 (where M represents Zn or Co). Liquid culture media were then prepared containing *M*-Fe(III)-oxyhydroxide (50 mM L^{-1}), acetate (20 mM), buffer ($NaHCO_3$, 30 mM) and an electron shuttle (Anthraquinone-2,6-disulfonate (AQDS); 10 μM). Separately, the Fe(III)-reducing bacterium *Geobacter sulfurreducens* was grown in a modified freshwater medium to late-log phase. The bacteria were concentrated into a pH neutral buffered suspension and added to the liquid culture media containing the metal doped suspensions. Through energy conservation, the bacteria combine the oxidation of the acetate (e^- donor) with the reduction of the *M*-Fe(III)-oxyhydroxide (e^- acceptor). Through this process, Fe(II) is released and recrystallizes with *M* and Fe(III) to produce the biogenic *M*-doped magnetite i.e. $M_xFe_{3-x}O_4$. Varying the concentration of *M* in the *M*-Fe(III)-oxyhydroxide ultimately determines the concentration of *M* in the final biogenic magnetite.

4.2 Preparation and characterization of the CA coating suspensions

Water-based nanoparticles suspensions were prepared by coating with citric acid (CA), as described in ref. [27], by conferring negative surface charge to the nanoparticles. Characterization of the colloids was performed using a Zetasizer 3000 (Malvern, U.K.). Stability of the citric acid coated nanoparticles in water was confirmed by zeta potential, which ranged between -30 mV and -50 mV, showing good stability of the negatively charged suspensions. Dynamic Light Scattering (DLS) characterization was also performed on the Zetasizer 3000 (Malvern, U.K.) at 25°C to determine hydrodynamic size of the coated individual/agglomerated nanoparticles in suspension.

4.3 Transmission Electron Microscopy measurements

Suspensions were deposited onto carbon/formvar coated copper TEM grids and examined using a JEOL 1230 TEM at an operating beam voltage of 100 kV. TEM of the CA coating was carried out using a Technai F20 electron microscope using an operating beam voltage of 200 kV and equipped with a field emission gun, EDX detector (Oxford Instruments) and Gatan SC600 CCD camera.

4.4 Calculation of the concentrations of the suspensions

Determination of the Fe content in the nanoparticles suspensions was obtained by Inductively Coupled Plasma (ICP) analysis, by digesting samples in high-purity nitric acid. Nanoparticles suspensions were mixed with concentrated nitric acid (70%) and heated at 60 °C for 48 hours. Resulting samples were diluted with deionized water (up to final 2% nitric acid) and 0.2 µm filtered. Complete digestion of unfiltered highly concentrated nanoparticles suspension was previously confirmed by DLS before and after digestion.

4.5 AC susceptibility

AC susceptibility measurements were performed using a home-built AC susceptometer operating at frequencies between 10 Hz and 220 kHz and 310 K. 200 µl of suspension were measured in each case. Absolute susceptibility values were obtained following background subtraction and calibration using a known mass of Dy_2O_3 powder.

4.6 Magnetic Hyperthermia

Magnetic hyperthermia measurements were performed using commercially available units supplied by nanoTherics Ltd in the frequency range of 87 kHz to 998 kHz. Calorimetric measurements were obtained on 1 ml of nanoparticles suspensions, using concentrations using concentrations determined by ICP analysis to be between 1.5 and 5 mg_{Fe}/ml, depending on the sample type. Control volumes of dH_2O and glycerol were measured to confirm that no heating occurred in the absence of nanoparticles. Glycerol-based nanoparticles suspensions for magnetic hyperthermia experiments were obtained by drying CA coated nanoparticles in water and resuspending them in glycerol (low heat assisted, ~ 50°C). The SAR was calculated from the initial slope of the heating curve.

AUTHOR INFORMATION

Corresponding Author

* Corresponding-Author: e.cespedes@keele.ac.uk

Present Addresses

† Present address: Fundación Imdea Nanociencia, Faraday 9, Cantoblanco 28049 Madrid, Spain

Author Contributions

The manuscript was written through contributions of all authors. All authors have given approval to the final version of the manuscript.

ACKNOWLEDGMENT

EC acknowledges the Ministry of Education of Spain for a postdoctoral grant at foreign research centers. The authors also thank K. Walker from the Electron Microscopy Unit of Keele University for her assistance.

ASSOCIATED CONTENT

Supporting Information Available: Supplementary information shows further details of the cluster model of polydisperse nanoparticles used for the AC susceptibility simulations. (**Figures S1** to **S3)**. Examples of the heating curves and the linear fit used to determine the SAR values are shown in **Figure S4**. **Figure S5** exhibits the energy loss per mass of iron during magnetic hyperthermia (from SAR values) normalized to H^2 and frequency for further comparison among samples. **Figure S6** shows the comparison between the simulations of AC susceptibility spectra including regions below and above the experimental frequency range for MN_A, $Zn_{0.2}$ and $Zn_{0.4}$ nanoparticles suspended in solvents with different viscosities (water, glycerol and a hypothetical high viscous solvent). **Figure S7** exhibits a comparison among the simulated χ" susceptibility of MN_A, $Zn_{0.2}$ and $Zn_{0.4}$ nanoparticles (a) in water and (b) in glycerol. This material is available free of charge via the Internet at http://pubs.acs.org.

REFERENCES

[1] K. Maier-Hauff, F. Ulrich, D. Nestler, H. Niehoff, P. Wust, B. Thiesen, H. Orawa, V. Budach, A. Jordan, *J. Neurooncol.* **2011**, 103, 317-24.

[2] B. Thiesen, A. Jordan, *Int. J. Hyperthermia* **2008**, 24, 467–474.

[3] A. Jordan, R. Scholz, K. Maier-Hauff, F. K. H. van Landeghem, N. Waldoefner, U. Teichgraeber, J. Pinkernelle, H. Bruhn, F. Neumann, B. Thiesen, A. von Deimling, R. Felix, *J. Neurooncol*. **2006**, 78, 7–14.

[4] K. Maier-Hauff, R. Rothe, R. Scholz, U. Gneveckow, P. Wust, B. Thiesen, A. Feussner, A. von Deimling, N. Waldoefner, R. Felix et al., *J. Neurooncol.* **2007**, 81, 53–60.

[5] M. Johannsen, U. Gneveckow, L. Eckelt, A. Feussner, N. Waldofner, R. Scholz, S. Deger, P. Wust, S. A. Loening, A. Jordan, *Int. J. Hyperthermia* **2005**, 21, 637–647.

[6] T. Kikumori, T. Kobayashi, M. Sawaki, T. Imai, *Breast Cancer Res. Treat.* **2009**, 113, 435–441.

[7] E. Alphandéry, S. Faure, O. Seksek, F. Guyot, I. Chebbi, *ACS Nano* **2011**, 5, 6279-96. doi: 10.1021/nn201290k.

[8] J. P. Fortin, C. Wilhelm, J. Servais, C. Ménager, J. C. Bacri, F. Gazeau, *J. Am. Chem. Soc.* **2007**, 129, 2628–2635.

[9] I. A. Brezovich, *Med. Phys. Monogr.* **1988**, 16, 82-111.

[10] R. Hergt, R. Hiergeist, M. Zeisberger, D. Schüler, U. Heyen, I. Hilger, W. A. Kaiser, *J. Magn. Magn. Mater.* **2005**, 293, 80–86.

[11] R. Hergt, S. Dutz, R. Muller, M. Zeisberger, *J. Phys.: Condens. Matter* **2006**, 18, S2919–S2934.

[12] E. Alphandéry, C. Carvallo, N. Menguy, I. Chebbi, *J. Phys. Chem. C* **2011**, 115, 11920-11924.

[13] E. Alphandéry, S. Faure, L. Raison, E. Duguet, P. A. Howse, D. A. Bazylinski, *J. Phys. Chem. C* 2**011**, 115, 18-22.

[14] J. Kolosnjaj-Tabi, R. Di Corato, L. Lartigue, I. Marangon, P. Guardia, A. K. A. Silva, N. Luciani, O. Clément, P. Flaud, J. V. Singh, P. Decuzzi, T. Pellegrino, C. Wilhelm, F. Gazeau, *ACS Nano* **2014**, 8, 4268-4283.

[15] A. K. Parchur, A. A. Ansari, B. P. Singh, T. N. Hasan, N. A. Syed, S. B. Rai and R. S. Ningthoujam, *Integr. Biol*. **2014**, 6, 53-64.

[16] A. I. Prasad, A. K. Parchur, R. R. Juluri, N. Jadhav, B. N. Pandey, R. S. Ningthoujam, R. K. Vatsa, *Dalton Trans.* **2013**, 42, 4885-96.

[17] P. Hugounenq, M. Levy, D. Alloyeau, L. Lartigue, E. Dubois, V. Cabuil,C. Ricolleau, S. Roux, C. Wilhelm, F. Gazeau, R. Bazzi*, J. Phys. Chem. C* **2012**, 116, 15702-15712.

[18] R.E. Rosensweig, *J. Magn. Magn. Mater.* **2002**, 252, 370–374.

[19] G. Vallejo-Fernandez, O. Whear, A. G. Roca, S. Hussain, J. Timmis, V. Patel, K. O'Grady, *J. Phys. D: Appl. Phys.* **2013**, 46, 312001-6.

[20] D. Ortega, Q. Pankhurst, Magnetic Hyperthermia. In Nanoscience: Volume 1: Nanostructures Through Chemistry, P. O'Brien, Royal Society of Chemistry: Cambridge **2013**, pp 60-88.

[21] R. Hergt, S. Dutz, M. Röder, *J. Phys.: Condens. Matter* **2008**, 20, 385214.

[22] G. Vallejo-Fernandez, O. Whear, A. G. Roca, S. Hussain, J. Timmis, V. Patel, K. O'Grady, *J. Phys. D: Appl. Phys*. **2013**, 46, 312001.

[23] A. P. Khandhar, R. M. Ferguson, K. M. Krishnan, *J. Appl. Phys.* **2011**, 109, 07B310, 1-3.

[24] R. Hergt, S. Dutz, M. Zeisberger, *Nanotechnology* **2010**, 21, 015706.

[25] V. S. Coker, N. D. Telling, G. van der Laan, R. A. D. Pattrick, C. I. Pearce, E. Arenholz, F. Tuna, R. E. P. Winpenny, J. R. Lloyd, *ACS Nano* **2009**, 3, 1922–1928.

[26] J. M. Byrne, N. D. Telling, V. S. Coker, R. A. D. Pattrick, G. van der Laan, E. Arenholz, F. Tuna, J. R. Lloyd, *Nanotechnology* **2011**, 201122, 455709.

[27] J. M. Byrne, V. S. Coker, S. Moise, P. L. Wincott, D. J. Vaughan, F. Tuna, E. Arenholz, G. van der Laan, R. A. D Pattrick, J. R. Lloyd, N. D. Telling, *J. R. Soc. Interface* **2013**, 10, 20130134.

[28] J. M. Byrne, V. S. Coker, E. Céspedes, P. L. Wincott, D. J. Vaughan, R. A. Pattrick, G. van der Laan, E. Arenholz, F. Tuna, M. Bencsik, J. R. Lloyd, N. D. Telling, *Adv. Funct. Mater.* **2013**, DOI: 10.1002/adfm.20130.

[29] E. Alphandéry, A. T. Ngo, C. Lefèvre, I. Lisiecki, L. F. Wu, M. P. Pileni, *J. Phys. Chem. C* **2008**, 112, 12304-12309.

[30] J. Sun, Y. Li, X.-J. Liang, P. C. Wang, *Journal of Nanomaterials* **2011**, 469031, doi:10.1155/2011/469031.

[31] S. Staniland, W. Williams, N. D. Telling, G. Van Der Laan, A. Harrison, B. Ward, *Nat. Nanotechnol.* **2008**, 3, 158-162.

[32] A. P. Herrera, L. Polo-Corrales, E. Chavez, J. Cabarcas-Bolivar, O. N. Uwakweh, C. Rinaldi, J. Magn. Magn. Mater. 2013, 328, 41–52.

[33] D. J. Craik, Intrinsic and technical magnetic properties of oxides, Wiley. London, UK, **1975** pp. 1–96.

[34] R. Di Corato R, A. Espinosa, L. Lartigue, M. Tharaud, S. Chat, T. Pellegrino, C. Ménager, F. Gazeau, C. Wilhelm, *Biomaterials* **2014**, 35, 6400-11.

[35] W. J. Atkinson, I. A. Brezovich, D. P. Chakraborty, *IEEE Trans. Biomed. Eng.* **1984**, 31, 70−75.

[36] R. Hergt, S. Dutz, J. *Magn. Magn. Mater.* **2007**, 311, 187−192.

[37] E. Mazario, N. Menéndez, P. Herrasti, M. Cañete, V. Connord, J. Carrey, *J. Phys. Chem. C* **2013**, 117, 11405-11411.

Table Captions

Table 1 (Top) Summary of structural and magnetic properties of most relevant biogenic samples. D is mean nanoparticle size; $\sigma_{(D)}$ is its dispersion index, D_H is mean hydrodynamic size, $\sigma_{(DH)}$ is its dispersion index, M_S RT is saturation magnetization at room temperature and K, magnetic anisotropy estimated considering uniaxial anisotropy. (Bottom) Structural and magnetic parameters from AC magnetic susceptibility simulations at 310 K of same samples. Values have been obtained from simultaneous simulation of experimental susceptibility spectra of each sample in water and glycerol, using same parameters in both except viscosity (η_{water} (310K) = (7 ± 0.5) x10^{-4} Pas, η_{glyc} (310K) = 0.35 ± 0.05 Pas).

Table 2 Summary of SAR for MN and $Co_xFe_{3-x}O_4$ samples suspended in water and in glycerol, at different frequencies ranging between 87 kHz and ~ 1MHz and at maximum magnetic field amplitude available. Δf = ± 5 kHz; ΔB = ± 0.5 mT.

Table 3 Summary of SAR for MN and $Zn_xFe_{3-x}O_4$ samples suspended in water and in glycerol, at different frequencies ranging between 87 kHz and ~ 1MHz and at maximum magnetic field amplitude available. Δf = ± 5 kHz; ΔB = ± 0.5 mT. Note that the maximum magnetic field for frequencies between 263 kHz and 740 kHz is larger than in **Table 2**, being the same for 87 kHz, 112 kHz and 998 kHz.

Figure Captions

Figure 1 TEM images of citric acid (CA) coated biogenic nanoparticles: magnetite nanoparticles (MNA) (a), Co-doped ferrite nanoparticles $Co_{0.4}$ (b) and $Co_{0.7}$ (c) and Zn-doped ferrite nanoparticles $Zn_{0.2}$ (d) and $Zn_{0.4}$ (e). Main micrographs (dispersed

NPs aggregates) correspond to highly diluted samples. Insets show concentrated NPs samples. An example of NPs cluster (from $Zn_{0.2}$) where CA coating can be distinguished is shown in (f) and high resolution TEM (from concentrated $Co_{0.4}$) as the inset.

Figure 2 (color on-line) (Top) Size distributions obtained from TEM measurement of n=500 particle diameters per sample of (a) magnetite nanoparticles, (b) Zn-doped ferrite nanoparticles and (c) Co-doped ferrite nanoparticles. (Down) Normalized number-weighted hydrodynamic size distributions of CA-coated nanoparticles suspensions ((d), (e) and (f), from (a), (b) and (c), respectively) obtained by Dynamic Light Scattering measurements.

Figure 3 (color on-line) AC Susceptibility simulations showing the evolution from pure Néel (a) to pure Brown (f) relaxation for a selected NP distribution (D = 15.5 nm, $\sigma_{(D)}$ = 0.2) with cluster distribution (D_H = 40 nm, $\sigma_{(DH)}$ = 0.30) by increasing anisotropy constant (K). Simulations have been done for water at 310 K ($\eta = 7 \times 10^{-4}$ Pa s).

Figure 4 (color on-line) (Top) Experimental AC susceptibility spectra of $Co_{0.7}$ (a) and $Zn_{0.2}$ (c) coated nanoparticles suspended in water and different mixtures of water-glycerol (in volume; 50%-glycerol, 75%-glycerol and 100% glycerol). (Bottom) AC susceptibility simulations of $Co_{0.7}$ (b) and $Zn_{0.2}$ (d) by using the parameters summarized in Table 1. Viscosity input values are η_{water} (310K) = (7 ± 0.5) $x10^{-4}$ Pas, $\eta_{50\%\text{-glyc}}$ (310K) = (4.5 ± 0.5) $x10^{-3}$ Pas, $\eta_{75\%\text{-glyc}}$ (310K) = (2 ± 0.5) $x10^{-2}$ Pas and η_{glyc} (310K) = 0.35 ± 0.05 Pas.

Figure 5 (color on-line) (a) Experimental AC susceptibility spectra of $Zn_{0.4}$ coated nanoparticles suspended in water and glycerol and their simulation (b) by using the parameters summarized in **Table 1** (bottom).

Figure 6 (a) Energy loss per cycle (mJ/g_{Fe}) during magnetic hyperthermia derived from SAR values measured in glycerol for MN_A and the Zn doped samples (b) Simulated χ" susceptibility of same samples in glycerol (using simulation parameters summarized in **Table 1**). Striped region shows the frequency range used for magnetic hyperthermia, from 87 kHz to 998 kHz.

Figure 7 SAR dependence versus applied magnetic field for (a) MN_B and (b) $Co_{0.7}$ in water at different frequencies. In the log-log plots, the dashed line corresponds to a square dependence of SAR on the field amplitude (slope = 2). SAR versus applied magnetic field for the two samples showing the highest experimental SAR values ($Co_{0.4}$ and $Zn_{0.2}$ in water at 87 kHz). (d) SAR versus magnetic field dependence for MN_A and $Zn_{0.2}$ samples suspended in glycerol.

Figure 8 T_2-weighted MR images for undoped magnetite (MN_A) and Zn-doped ferrites $Zn_{0.2}$ and $Zn_{0.4}$ in comparison with a standard MRI contrast agent (Feridex®), for two different nanoparticles doses.